Picosecond wide-field magneto-optical imaging of magnetization dynamics of amorphous film elements

Babak Mozooni, Thomas von Hofe, and Jeffrey McCord*
Institute for Materials Science, University of Kiel, Kaiserstraße 2, 24143 Kiel, Germany
(Received 3 April 2014; revised manuscript received 28 July 2014; published 15 August 2014)

Time-resolved wide-field magneto-optical microscopy with picosecond time resolution and with phase-locked harmonic excitation is used to image the fundamental dynamic modes of magnetic domain and domain-wall states in soft-magnetic thick film elements. By analyzing mirrored domain states, the pure in-plane and out-of-plane dynamic magnetic response under a continuous microwave excitation is extracted simultaneously. Domain-wall oscillations and local domain response, including transversely aligned and closure domain states, are visualized below, at, and above the resonance frequency of the magnetic elements. Regions of different high-frequency permeability are distinguished from the laterally resolved measurements. Despite nearly constant precessional frequency, a strong mode amplitude variation is found with varying the magnetic bias field, which is correlated to the exhibited change of the individual domain structure. Inhomogeneous out-of-phase precessional modes within the individual domains occur close to a state of domain instability. The imaging results are compared to existing models of flux response. Magnetic domain knowledge and precise dynamic imaging is needed for the understanding of the dynamic magnetization behavior of even basic domain structures beyond the magnetic material's elementary properties.

DOI: 10.1103/PhysRevB.90.054410 PACS number(s): 75.60.Ch, 75.40.Gb

I. INTRODUCTION

The knowledge of fast magnetization reversal processes in magnetic elements is a key parameter for many new technologies and applications such as magnetic random access memories and spintronic devices [1]. Other envisioned applications are magnonic crystals, using periodically structured magnetic films to transmit and process magnetic spin waves [2–4]. Despite the projected applications, many of the physical aspects behind the proposed magnetic devices are still a focus of current research. Yet, the understanding of the details of magnetization dynamics of magnetic structures on the micrometer scale are relevant for applications like microinductors [5–9] and magnetic recording heads [10–14], relying on micrometer-sized large-scale magnetic elements. So far magnetodynamic aspects of such large structures are not easily accessible by micromagnetic calculations. Moreover, magnetic thick films structures with thicknesses above 100 nm that exhibit an asymmetric Bloch domain-wall structure are employed in that case.

In general, the dynamic magnetic behavior of magnetic structures is related to the precessional or resonance frequency f_{res} and the damping parameter α of the materials. The precessional motion of magnetization subjected to an effective magnetic field H_{eff} is described by the Landau-Lifshitz-Gilbert (LLG) differential equation [15]

$$\frac{\partial M}{\partial t} = -\gamma M \times H_{\mathrm{eff}} + \frac{\alpha}{M_{\mathrm{s}}}\left(M \times \frac{\partial M}{\partial t}\right), \qquad (1)$$

where M_{s} is the saturation magnetization, and γ the gyromagnetic ratio. The first term in Eq. (1) describes the precession of the magnetization M with a characteristic precession or resonance frequency f_{res} depending on the effective field H_{eff} acting on M. The second term in Eq. (1) corresponds to the phenomenological damping torque, which is responsible for the orientation of magnetization into the equilibrium state, described by the damping parameter α.

However, due to local demagnetization effects, the exhibited magnetic domain structure, and also due to the domain-wall structure, the effective dynamic response is altered in a complicated way [16–22]. The magnetization vector $\vec{M}$ is distributed inhomogeneously and aligned nonorthogonal relative to an applied microwave field. A reduction in high-frequency permeability with exhibited domain structures is usually explained by a reduction of active magnetic volume. The most detailed theoretical discussion on the possible effects is presented in Ref. [19], in which a detailed domain model for the magnetization dynamics in soft-magnetic film elements is described. In the model, the domain system is treated as a nonlinear system of coupled viscously damped (magnetic) oscillators with geometrically constrained motion. Depending on the excitation frequencies, different regions on the film element are predicted to respond to the magnetic radio-frequency (rf) field excitation. The magnetodynamic response is then limited ultimately by classical eddy current damping of the magnetization rotation or the precessional frequency in the center of the patterned soft-magnetic elements. Experimentally, it was found that rf flux propagation is not limited to the center of the element, but also partial magnetization rotation in the regions enclosed by the closure domains occurs [21].

In general, the modeling results appear to be in line with experimental results obtained from integral measurements, i.e., from experiments which measure the overall magnetic response of the entire object. On the other hand, for relatively large nearly saturated magnetic elements, spin-wave modes are known to be localized near the center of the element along the direction of main magnetization, the nature of the modes being purely dipolar [23–25]. In order to obtain a clear picture of the magnetic dynamic response, the switching mechanisms and possible spin-wave localizations in such materials must

*jmc@tf.uni-kiel.de

be investigated by using laterally resolved techniques with high temporal resolution. So far, various efforts have been made to image and analyze the high-frequency response of magnetic films on the subnanosecond time scale, using a variety of different methods based on magneto-optics or x rays [26–29]. Each method possesses advantages in terms of temporal and lateral resolution, as well as limitations related to the experimental conditions.

The optical methods are based on the application of the magneto-optical Kerr effect (MOKE). The primary established time-resolved imaging method is scanning Kerr microscopy, using nanosecond, picosecond, or femtosecond pulsed laser systems [24–26,30,31]. Yet, despite advantages in image acquisition time and higher flexibility in terms of field of view, wide-field Kerr microscopy [32,33] is rarely used. One of the reasons for this lies in the difficulties to obtain a good signal-to-noise ratio due to the occurrence of laser speckle, the residual contrast of which can conceal the low magneto-optical contrast. Imaging of domain (-wall) influences in large-scale elements on the magnetization dynamics by time-resolved magneto-optical methods was so far mostly performed by pulsed field excitation. From complementary integral rf magnetometry it was found that the dominating ferromagnetic resonance modes also depend directly on the domain-wall density and correspondingly on the domain width. Until now, the individual precessional modes inside the elements and the individual domains of different characters were not investigated.

Here, quasi-jitter-free time-resolved wide-field Kerr microscopy with picosecond resolution is used to investigate the local magnetic domain and domain-wall response of amorphous magnetic film elements at fixed frequencies. The paper is organized as follows: First, the experimental methods with a strong focus on the picosecond wide-field Kerr microscopy method with phase-locked harmonic excitation are introduced, by which pure in-plane rf magnetization response is obtained. Next, the lateral response of a Landau-type domain structure to magnetic single-frequency rf fields is analyzed. Details of the lateral magnetic domain and domain-wall response are derived. By using additional and complementary quasistatic and dynamic measurement techniques, a complete picture of the lateral varying magnetodynamic processes up to several GHz is obtained.

II. EXPERIMENT

The sample investigated is a patterned $(Fe_{90}Co_{10})_{78}Si_{12}B_{10}$ amorphous ferromagnetic film sputtered on a transparent glass substrate with a magnetic layer thickness of 160 nm, thereby in the asymmetric Bloch-wall regime [34]. A uniaxial anisotropy is introduced to the material during the sputtering process by applying a magnetic field of $H_{dep} = 10$ mT [35]. By using optical lithography, the sample is patterned into an array of 40 μm $\times$ 40 μm square elements with a 10-μm gap between each element, ensuring magnetostatic decoupling between the individual elements.

The dynamic magnetic response of the sample is measured by pulsed inductive microwave magnetometry (PIMM) [36] with varying bias fields, from which dynamic magnetic permeability spectra were obtained. For all the dynamic measurements, the sample is placed upside down on the center of a coplanar waveguide with a bandwidth above 15 GHz. By varying the magnetic bias fields H_{bias}, the dynamic response is directly compared to the varying magnetic domain structures. The PIMM data have been extracted after initializing the sample along its easy axis of magnetization, thus ensuring well-defined and comparable conditions for all (to follow) measurements. The dynamic response was further investigated from the variation of the transmission amplitude of the microwave signal in a two-port configuration in dependence of the frequency, basically measuring the amount of magnetic loss as a function of rf excitation frequency. The overall magnetic domain structure of the array structure is imaged by quasistatic magneto-optical Kerr microscopy with varying magnetic fields [34,37].

III. DYNAMIC MAGNETIC IMAGING METHOD

The lateral dynamic response is imaged by stroboscopic time-resolved wide-field Kerr microscopy. A systematic sketch of the imaging setup is displayed in Fig. 1. High temporal resolution is achieved by using a mode-locked diode-pumped and frequency-doubled Nd:YVO_4 laser ($\lambda = 516$ nm) with a pulse width of 7 ps and a fixed repetition rate of 50 MHz as an illumination source. A typical average output power of about 150 mW is obtained. The laser light is coupled to the microscope through a multimode optical fiber. Sensitivity to in-plane and out-of-plane magnetization components is achieved by focusing the fiber output on the back focal plane of the objective lens. By adjusting the position of the fiber output, the plane of incidence and the sensitivity axis are set [38], and hence out-of-plane (polar) plus in-plane (longitudinal) magneto-optical contrast is obtained. For all investigations, the sample is placed upside down on a coplanar waveguide for rf field excitation. In order to focus on the sample, an

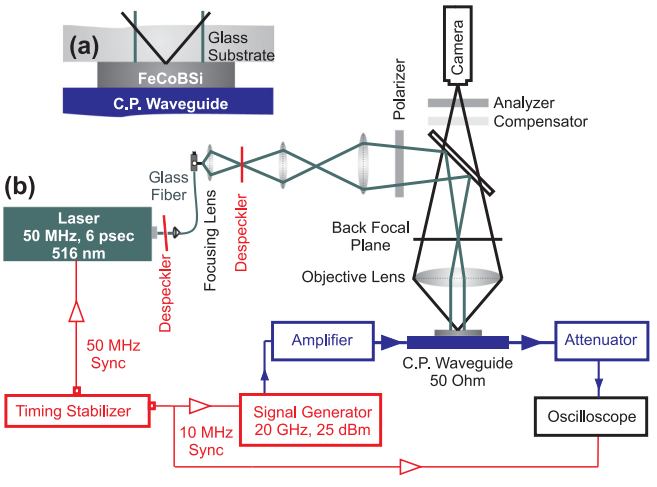

FIG. 1. (Color online) (a) Sketch of sample design and (b) experimental imaging setup consisting of a mode-locked laser as an illumination source, a magneto-optical Kerr microscope, and a rf magnetic field excitation source. The mode-locked Nd:YVO_4 laser runs from the same clock as the high-power rf signal generator, ensuring quasi-jitter-free imaging. A computer (not shown) is used to control the experiment and to record the CCD camera image.

objective lens with a correction ring is used, providing the ability of focusing onto the ferromagnetic film surface through the glass substrate. With a numerical aperture of NA = 0.5, the lateral resolution is limited to around 400 nm in the presented experiments.

A rf signal generator with a bandwidth of 20 GHz is used for generation of the rf magnetic field. Optionally, an amplifier with a bandwidth of 4 GHz and the maximum power of 5 W can be incorporated into the imaging setup. The rf signal is sent through a narrow impedance matched (50-Ω) coplanar waveguide with a width of 150 μm. Both the signal generator and the laser are running from the same reference signal, whereas the 50-MHz clock for the laser system is derived from higher harmonics of the 10-MHz clock signal for the rf field excitation source. The clock synchronizer feedback system results in timing jitter of less than 0.5 ps.

Images are obtained with a rf field by applying a base-to-peak voltage amplitude of 4 V, corresponding to a rf in-plane magnetic field excitation $H_{\mathrm{rf}} \approx 0.3$ mT acting on the sample [32]. The temporal and laterally resolved data of the magnetization response thereby allow for the separation of domain and domain-wall-induced effects up to several GHz excitation frequencies. The time-resolved imaging is performed in a stroboscopic differential imaging mode with varying the phase between the rf field excitation and the imaging laser pulse. Individual differential images (Δ) are obtained from the difference of two magnetization states with a phase shift differing by π, i.e., the first image is taken at a certain ac field phase φ and then by shifting the field phase by π the second image is obtained at $\varphi + \pi$. By imaging in this manner, only changes of magnetization become visible. To monitor the voltage signal and to control the timing of the experiment, the output of the coplanar waveguide is detected by a high-bandwidth sampling oscilloscope.

Exemplary quasistatic domain images and dynamic imaging data from the magnetization responses of two adjacent magnetic elements at a 3-GHz excitation field are displayed in Fig. 2. The static images with vertical plane of incidence [Fig. 2(a)] and corresponding differential dynamic response images for perpendicular [Fig. 2(b)] and oblique plane of incidence [Fig. 2(c)] are compared. The shown dynamic domain response images obtained from the difference between domain states of a phase difference of $\Delta\varphi = \pi/2$ are selected for maximum magneto-optical response. Clearly, a locally varying magnetization response within the magnetic elements is seen. Whereas the contrast interpretation of perpendicular plane of incidence (polar) Kerr sensitivity images is straightforward, the sensitivity for oblique plane of incidence is sensitive to in-plane (longitudinal) and additionally out-of-plane (polar) components of magnetization. In magneto-optical imaging of soft-magnetic samples, often pure in-plane alignment of magnetization is assumed, a presumption that is not valid for precessional motion of magnetization at high frequencies. An indication of a mixed magnetization response becomes visible by comparing the opposite magneto-optical response contrast [Fig. 2(b)] of the central domains. In order to extract the in-plane and out-of-plane magnetization response from one set of oblique plane of incidence images, the magnetic response for two equivalent, but inverted, domain structures is analyzed simultaneously. The average MOKE response

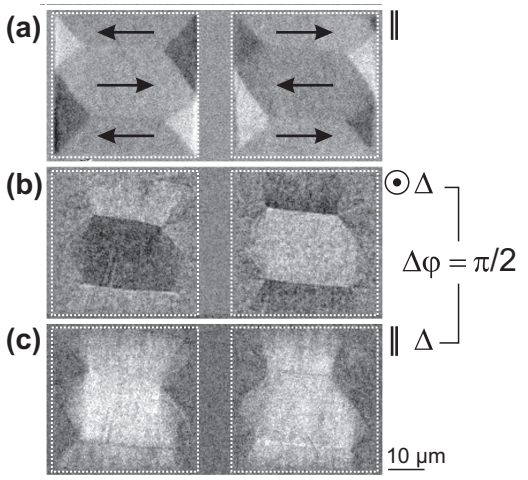

FIG. 2. (a) Exemplary quasistatic magnetic domain images and corresponding dynamic domain response images for two neighboring magnetic elements with a nearly mirrored domain structure for (b), displaying only out-of-plane as well as (c) combined out-of-plane and in-plane sensitivity. The planes of incidence (⊙, ∥) that define the sensitivity directions are indicated. Mirrored domain states are obtained by demagnetizing the sample in an alternating in-plane magnetic field with decreasing amplitude along the easy axis of magnetization, starting from magnetic saturation.

from each individual domain is extracted individually. From symmetry considerations, the longitudinal (in-plane) MOKE response of precessional motion is derived from the sum and the polar (out-of-plane) response from the difference of individual domain response of an equivalent mirrored domain structure.

Figure 3 shows the evolution of magneto-optical contrast within the center domain after applying a 3-GHz rf excitation field. In Figs. 3(a) and 3(b), the obtained magneto-optical in-plane contrast from oppositely aligned domains of the two mirrored domain structures has similar intensity but a slight phase shift, as the magneto-optical sensitivity contains both longitudinal and out-of-plane contrasts. In order to extract the pure longitudinal in-plane and polar contrast change, the obtained intensities shown in Figs. 3(a) and 3(b) have been added [Fig. 3(c)] and subtracted [Fig. 3(d)], respectively. Comparing the resulting longitudinal and polar magneto-optical signal, and in accordance with the precessional motion, a phase shift of $\pi/2$ in the magnetization response is obtained. (The longitudinal in-plane response of Fig. 3(c) is added in Fig. 3(d)]. Moreover, the central domain response of the mirrored domain structures is analyzed with polar magneto-optical (out-of-plane) sensitivity, the results of which are displayed in Figs. 3(e) and 3(f). An antiphase magnetic response for oppositely aligned magnetization is obtained, again in accordance with the precessional nature of response. Deviations in signal amplitude and from an exact antiphase behavior are attributed to small longitudinal MOKE contributions and a slight gradient of MOKE sensitivity across the field of view. The complementary polar magneto-optical analysis affirms the methodology, which *is* used for the following laterally resolved analysis at multiple excitation frequencies from 50 MHz up into the GHz regime.

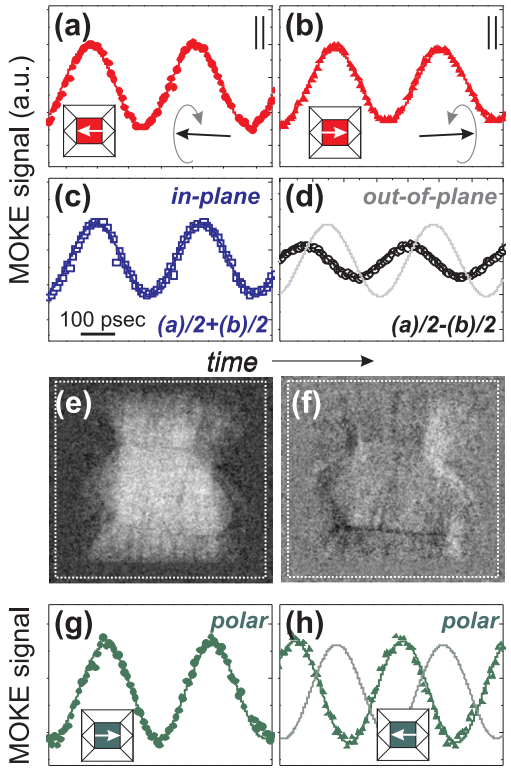

FIG. 3. (Color online) Time evolution of magneto-optical contrast obtained from image intensity analysis of the sample exposed to a 3-GHz rf field. (a), (b) Magneto-optical contrast obtained with oblique plane of incidence (‖) from domains aligned perpendicular to the excitation field, but aligned oppositely. (c) The averaged intensity of domains contrasts [(a)/2 + (b)/2, pure longitudinal component]. (d) The subtracted intensity of domains contrasts [(a)/2 − (b)/2, pure polar component]. The same scale for the MOKE signal is used in (a)–(d). (e) Constructed longitudinal response image by summing up two mirrored domain states (corresponding to pure in-plane sensitivity). (f) Constructed polar response image by subtracting of mirrored domain states (corresponding to pure polar contrast). (g) Polar magneto-optical contrast obtained directly from the out-of-plane sensitivity of microscope (right domain). (h) Polar magneto-optical contrast obtained from out-of-plane sensitivity of the microscope (right domain). The nearly antiphase contrast from the precessional response of (g) is included in (h). The same scale for the MOKE signal is used in (g) and (h).

IV. RESULTS

The evolution of the magnetic domain distribution with easy-axis (e.a.) magnetization reversal is displayed in Fig. 4. The magnetic domain images for increasing magnetic fields Figs. 4(a)–4(i) show that above $H_{\text{bias}} = -4$ mT magnetic domains start to nucleate from the edges of the magnetic elements [Fig. 4(a)–4(b)]. With decreasing field, a seven-domain state develops. The magnetization reversal then proceeds by continuous domain-wall motion over a wide magnetic field range [Figs. 4(b)–4(h)]. Around $H_{\text{bias}} = 4$ mT [Fig. 4(h)–4(i)] the domain walls, which are now positioned in the cental part of the magnetic elements, annihilate. For the e.a. reversal, the magnetization distribution displays almost no hysteresis, only at high magnetic fields signs of domain nucleation are found.

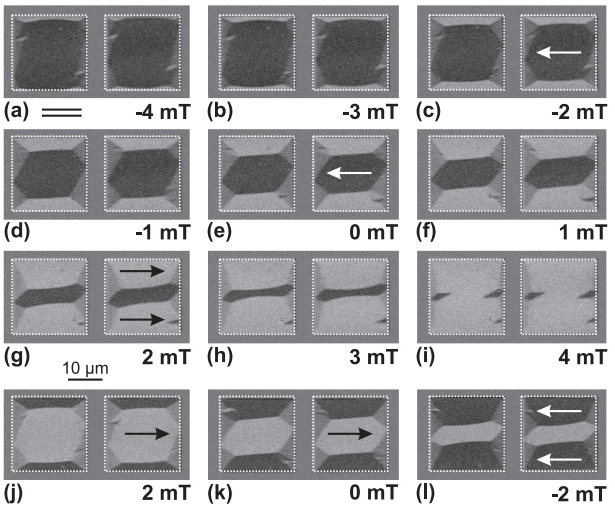

FIG. 4. Exemplary magnetic domain images obtained for the easy-axis magnetization reversal. (a)–(i) are obtained from the forward loop and (j)–(l) from the backward branch of the magnetization loop. Magnetic field values and directions of magnetization are indicated.

Nevertheless, the occurring domain patterns are hysteretic in nature. Exemplary domain images for the decreasing field values are displayed in Figs. 4(j)–4(l). Due to the domain formation process with field, the magnetization distribution is reversed, which becomes clear comparing domain images from the forward and backward loops [compare Figs. 4(c) to 4(j), 4(e) to 4(k), and 4(g) to 4(l)]. The formation of domains and the field dependency of the magnetic domain structures also alter the dynamic magnetization behavior.

The dynamic magnetic permeability spectra maps for increasing and decreasing magnetic fields along the e.a. of magnetization are shown in Fig. 5(a). For high-bias field amplitudes a Kittel-type $f_{\text{res}}^2 \sim \pm H_{\text{bias}}$ [39] behavior is observed [Fig. 5(b)]. In the intermediate field range (-4 mT $< H_{\text{bias}} <$ $+4$ mT), in connection with the occurrence of the multidomain state (compare to Fig. 4), the dominating precessional frequency $f_{\text{res}} \approx 3$ GHz remains approximately constant. Constant f_{res} dependencies for soft-magnetic elements with field biasing are reported in Ref. [21]. Yet, by comparing f_{res} for increasing and decreasing magnetic fields, signs of a hysteretic nature of the process become visible. Despite the similar value of precessional frequency, the permeability peak amplitude changes strongly with H_{bias} [Fig. 5(c)] and the alteration of the magnetic domain structure (see Fig. 4). The permeability amplitude $|\mu|$ peaks at the point of domain annihilation. The contributing effects of the magnetic domain structure on the local dynamic response of magnetization are analyzed by time-resolved magneto-optical microscopy. The general correspondence between the pulsed field (PIMM) results and the magneto-optical microscopy with phase-locked field excitation is further checked from the variation of the transmission amplitude of the rf signal under identical conditions as the magneto-optical imaging. In accordance with the PIMM data, the maximum the precessional frequency peak $f_{\text{res}} \approx 3$ GHz matches the results of the experiments with harmonic field excitation (not shown).

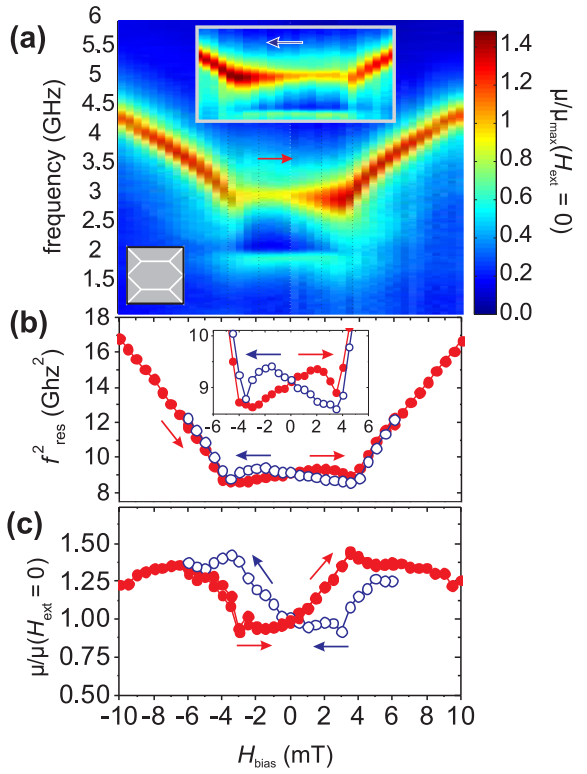

FIG. 5. (Color online) (a) Amplitude permeability spectra map obtained from PIMM measurements for increasing magnetic field values. The inset displays the corresponding section for decreasing field values. (b) Dominating precessional frequency square f_{res}^2, and (c) normalized peak permeability $|\mu|/|\mu(0)|$ versus H_{ext}.

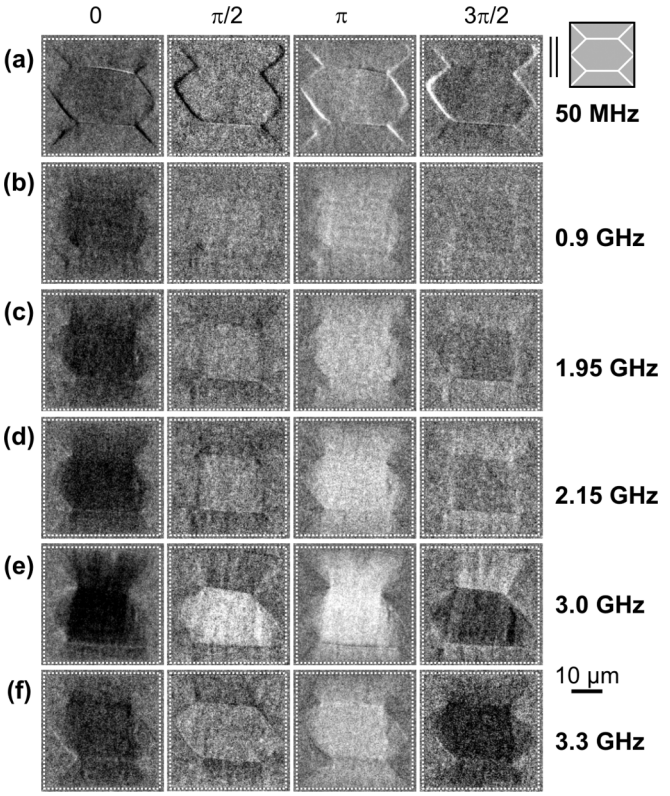

FIG. 6. Exemplary laterally resolved magnetic response images for oblique plane of incidence at (a) 50 MHz, (b) 0.9 GHz, (c) 1.95 GHz, (d) 2.15 GHz, (e) 3.0 GHz, and (f) 3.3 GHz. The phase of the excitation field is shown in steps of $\pi/2$ (as indicated). The relative MOKE image contrast is increased for a phase of $\pi/2$ and $3\pi/2$ relative to 0 and π by a factor of 1.5.

Exemplary time-resolved differential images for oblique plane of incidence for different frequencies with varying delay are shown in Fig. 6. The delay, corresponding to a phase shift of $\pi/2$ between the shown differential images, varies from 5 ns [Fig. 6(a)] to 76 ps [Fig. 6(f)], corresponding to an excitation frequency of 50 MHz and 3.3 GHz, respectively. For 50-MHz field excitation, the magnetic response occurs by homogeneous rotation of magnetization in the domains with the magnetization aligned perpendicular to the rf field, and to a high degree by 90° domain-wall motion. Moreover, the wall motion process is hysteretic, visible from the still existing domain-wall contrast at $\pi/2$ and $3\pi/2$ in Fig. 6(a).

The magnetization rotation in the central part of the element increases constantly with frequency and peaks around f_{res} as determined from the inductive measurements [Fig. 6(e), 0 and π]. Also, at f_{res} the strongest out-of-plane magneto-optical contributions become visible, exhibiting an alternating domain contrast for $\pi/2$ and $3\pi/2$ [Fig. 6(e)]. Using the MOKE signal separation scheme discussed above, the out-of-plane and in-plane magnetization contributions are separated. An analysis of the latter for three selected excitation frequencies is shown in Fig. 7. The in-plane magnetization response increases by a factor of 3 for the shown frequency range.

A complete analysis of the different contributions of in-plane and out-of plane magnetization contributions for the different domain regions is given in Fig. 8, from which a quantitative comparison of paths of flux propagation becomes possible. The contribution of precessional motion of magnetization is derived from the out-of-plane change of magnetization. At low frequencies ($f_{\mathrm{rf}} = 0.9$ GHz), the average precessional motion is almost equal for all domains with the magnetization aligned perpendicular to the excitation frequency. With increasing frequency, the local polar response

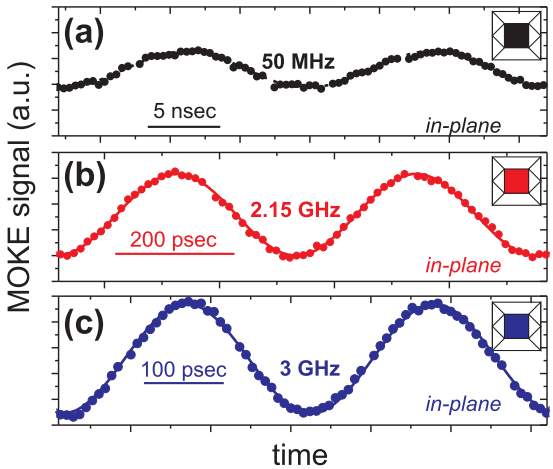

FIG. 7. (Color online) Central domain magnetization response for (a) 50 MHz, (b) 2.15 GHz, and (c) 3.0 GHz. The position of the central domain is indicated. The vertical axes have the same scale.

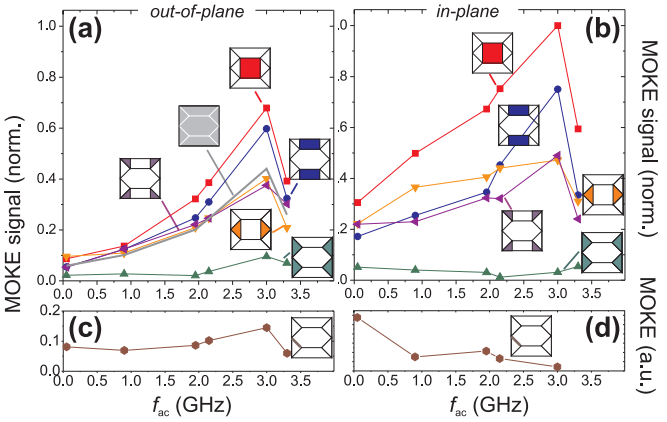

FIG. 8. (Color online) Dependence of local (a) out-of-plane and (b) in-plane magnetization response with excitation frequency. The corresponding change of 90° domain-wall contrast is displayed in (c) and (d). The regions of domains are indicated.

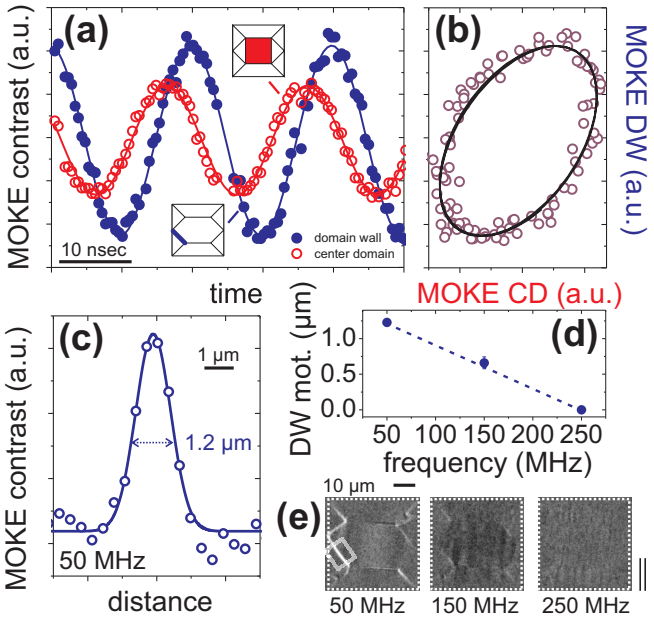

FIG. 9. (Color online) (a) Time evolution of the oblique plane of incidence MOKE signals from the center domain and from one domain wall (position as indicated) for 50-MHz field excitation. (b) Plot of the individual MOKE signals related to the domain-wall displacement over the MOKE response from the center domain [same data as in (a)]. (c) MOKE intensity plot across a domain wall from a differential image displaying the magneto-optical track of the moving domain wall. (d) Derived domain-wall displacement with excitation frequency and (e) corresponding domain images.

strongly increases, peaking for all domains at $f_{rf} \approx 3$ GHz. The strongest out-of-plane precession is obtained in the central domain [red, Fig. 8(a)]. The closure domain structures at low frequencies display no precessional motion. However, at higher frequencies and with increase of precessional motion in the neighboring domains, also in the closure domain structures [green, Fig. 8(a)] precessional motion takes place through magnetostatic coupling to the neighboring domains. No corresponding in-plane magnetization response occurs in the closure domains [green, Fig. 8(b)]. By this, and despite the occurrence of precession of magnetization, the closure domains are not contributing to magnetic flux propagation. The in-plane response in the "wing" of the central domain is of special interest [orange, Fig. 8(b)]. Together with the central region [red, Fig. 8(b)] and the surrounding edge domains [blue, Fig. 8(b)], the flux response increases in a similar way up to $f_{rf} \approx 1$ GHz. With further increasing f_{rf}, the signal in the narrow wing area is only slowly increasing and the flux is channeled into the central edge domain above and below the central domain. By this, the magnetization response in the top and down edge domains increases disproportionately between $f_{rf} = 2$ and 3 GHz.

The in-plane domain-wall contrast reduces above 50-MHz excitation, confirming the absence of domain-wall movement in the GHz regime [Fig. 8(d)]. Nevertheless, at $f_{rf} = f_{res} = 3$ GHz with domain resonance, out-of-plane precessional magnetization components are detected [Fig. 8(c)]. This indicates the precessional motion of magnetization inside the domain wall. Out-of-plane magnetization components changing with the excitation frequency, which indicate a structural change of the magnetization distribution, become also visible at the asymmetric 180° Bloch walls. (No out-of-plane components of magnetization are detectable in the quasistatic measurements.) The structural modification of the asymmetric Bloch walls at higher excitation frequencies was predicted from micromagnetic calculations [40]. Already at $f_{rf} \approx 50$ MHz a phase shift of the domain-wall motion relative to the excitation (or a hysteresis in the domain-wall motion) can be derived from the analysis of the domain-wall contrast of the time-resolved MOKE images, the data of which are shown in Figs. 9(a) and 9(b). The overall distance of domain-wall motion is derived from the maximum half-peak-width [Fig. 9(c)] of the MOKE intensity across a 90° domain wall obtained from the differential images. For increasing excitation frequencies, the domain walls are not able to completely follow the rf field excitation. Despite the increase in excitation frequency, the domain-wall movement is decreasing [Fig. 9(d)]. From the average distance swept by the domain wall, a wall velocity $v_{DW} \approx 60$ m/s is derived for f_{rf} 50 MHz. No domain-wall motion is visible in the domain images [Fig. 9(e)] for frequencies of 250 MHz and above (see also Fig. 6). Changing the shape of the magnetic domains, but still keeping the seven-domain state is achieved by applying magnetic bias fields along the e.a. of magnetization (see also Fig. 4). The relative change of magneto-optical signal with oblique plane of incidence at resonance for the central domain and the domains next to the edges for three different magnetic domain states corresponding to Figs. 4(c), 4(e), and 4(g) are compared in Fig. 10. As these images all contain longitudinal and polar MOKE contributions, the interpretation of the MOKE signal dependency is not easy. With field biasing, no mirrored domain states to separate the MOKE signal contributions exist. The local magnetic signal response is shown in Fig. 10(a). The central domain response increases with the decrease of domain width. This is apparently not matching the expectation that the domain width, or a dynamic demagnetization effect [21,41,42], is the dominating factor in determining changes of effective dynamic magnetic anisotropy. Nevertheless, this interpretation

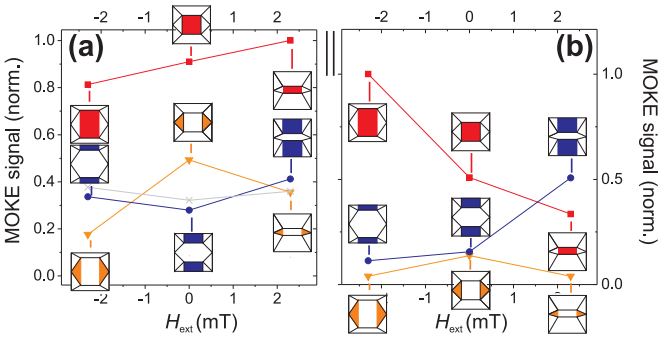

FIG. 10. (Color online) (a) Dependence of local oblique plane of incidence MOKE signals for three exemplary flux delivering regions for different external magnetic bias fields. (b) Contributing MOKE signals weighted relative to the surface area. The individual regions of domains are indicated.

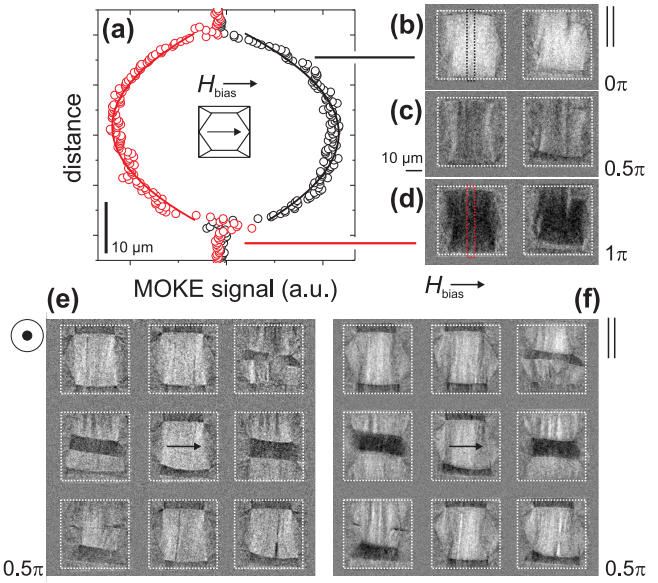

FIG. 11. (Color online) (a) MOKE signal variation across the magnetic elements for maximum and minimum magnetic field excitations. MOKE images for (b) maximum, (c) intermediate, and (d) minimum MOKE signals. The regions from which the line plots in (a) are derived are indicated in (b) and (d). Exemplary images of the same domain structures obtained with (e) polar MOKE sensitivity and (f) oblique plane of incidence.

was mainly derived from the analysis of elongated stripe structures. For the square elements investigated here, and for all smaller element shapes, the local demagnetization field distribution and the occurrence of magnetostatic Damon-Eschbach modes [43] have to be considered [23,24,44]. They result in a higher excitation in the center of the element and overlap the domain-size effect. The corresponding signal from the wing domains, which are surrounded by the closure domains, first slightly increases and then decreases again. The local MOKE response from the edges [blue, Fig. 10(a)] decreases with increasing magnetic bias field and increasing domain width. The overall magnetic response contribution is derived by taking the individual sizes of the domains into account [Fig. 10(b)]. Due to the changes of the individual domain areas, the main impacts shift from the central domain to the two adjacent edge domains with increasing magnetic bias field. The overall contribution of the wing domains peaks for zero-bias magnetic fields.

Already indicated above, the distribution of MOKE response is not homogeneous within the element and especially not homogeneous within the individual domains. An example for the evolution of magnetization response at $f_{rf} = 3$ GHz across the element for high-bias fields approaching the point of domain annihilation ($H_{bias} \approx 3$ mT) starting from a demagnetized state with a large center domain is plotted in Fig. 11(a), the corresponding magnetic domain images of which are displayed in Figs. 11(b) and 11(d). Maximum response in the center domain is achieved in the center of the element, gradually decreasing to the edge regions. This dependency is similar to a magnetostatic Damon-Eschbach mode, but limited to only one magnetic domain. The fits displayed in Fig. 11(a) are performed by assuming a simple sinusoidal function. Higher-wavelength modes were not included. Moreover, best noticeable in Fig. 11(c), dynamic modes along the aligned magnetization occur. The response within the domain is irregular and varies from element to element. From comparative studies on other elements we find a strong connection, respectively interaction of the irregular dynamic modes to the surrounding domain walls in the system, a few representative examples of which are shown for different sensitivity directions in Figs. 11(e) and 11(f). The observed modes display characteristics similar to ripplelike magnetic domain structures. Strong interaction with sample edges and domain walls are visible from the dynamic images. With slightly increased amplitude of excitation, domain switching processes are observed. The occurrence of the dynamic modes appears to be related to the occurrence of microwave [45,46] induced switching of the magnetic domain structures, even without any magnetic bias field, leading to an instantaneous switching of the magnetic seven-domain state into the mirrored or inverted domain state.

V. DISCUSSION

A general description of fast magnetization processes in patterned films was presented in Ref. [16]. There, a model for charge-free flux transfer by pure rotation in magnetic structures is proposed. The model is based on experimental data from integral measurements [47]. In the model, the rf response takes place through flux propagation limited to the center of the magnetic element [Fig. 12(a)]. The effective permeability in the closure domain regions at the elements edges is negligible. A similar model for high-excitation frequencies was proposed by Smith [19], which added more details to the magnetization dynamic behavior. In accordance with the experimental data shown here, a progressive reduction of the wall-motion amplitude occurs above 10 MHz. A transformation from domain-wall-dominated to rotation-dominated magnetization reversal around $f_{rf} = 100$ MHz was predicted by the model. The rolloff of domain-wall motion is explicitly confirmed by the presented investigations.

An alternative model was suggested in Ref. [17], in which the flux propagation is not only limited to the center of the

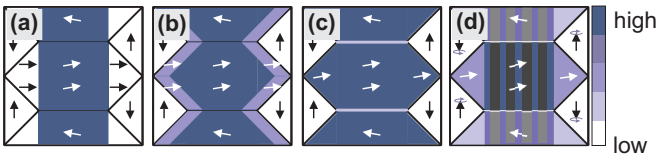

FIG. 12. (Color online) High-frequency flux transfer mechanisms in patterned soft-magnetic elements according to (a) Mallary [16] and Smith [19], (b) Ohashi [17], (c) Queitsch *et al.* [21], and (d) from the presented results. The regions with flux propagation, respectively higher magnetization rotation, are highlighted. Areas with different dynamic permeability are indicated (see text for details, darker colors indicate regions of higher rf permeability).

element, but also magnetization rotation inside the closure domain regions is assumed [Fig. 12(b)]. In the model the rf permeability is lowered in regions close to the 90° domain walls. No response of magnetization in the closure domains themselves takes place for both models.

Common to both models, the permeability in the cental part of the elements is determined by the anisotropy field H_k of the material. However, domain observation data obtained by applying pulsed field excitation [21] showed that the dominating ferromagnetic resonance modes depend also on the domain-wall density due to the narrow region of reduced permeability forming at the 180° domain walls as sketched in Fig. 12(c). No reduction of permeability in the regions surrounded by the closure domain was found. All models and data were obtained from the analysis of extended stripe structures or elongated elements.

Our time-resolved domain investigations prove that the magnetization processes in large-scale elements are more complicated as predicted from the domain models. Experimental results from pulsed magnetic field excitation on elongated elements [Fig. 12(c)] are only able to describe a few aspects of the occurring magnetodynamic effects. A sketch summarizing the local magnetodynamic response at the precessional frequency of the elements, which is based on the presented work, is shown in Fig. 12(d). Noticeably, the closure domains contribute to the dynamic response due to magnetostatic coupling by magnetization precession. The rf permeability in the central top and down domains is reduced relative to the central domain. At resonance, inhomogeneous dynamic modes occur inside the domains. Based on the imaging results, existing models of flux response must be refined. Most of the observed differences are due to precessional out-of-plane magnetization contributions, which were not included in the early models.

VI. SUMMARY

By performing time-resolved wide-field Kerr microscopy with phase-locked harmonic excitation we were able to identify different fundamental magnetodynamic modes in magnetic thick film elements, exhibiting a simple Landau-type domain structure. Imaging is performed in a way to distinguish in-plane and out-of-plane dynamic response from a single MOKE wide-field measurement with oblique incidence of light, separating the polar and longitudinal MOKE signals.

Starting from the magnetic ground state, the lateral magnetic flux paths under continuous microwave magnetic field excitation in the magnetic element were identified for different frequencies. Areas of differing high-frequency permeability are distinguished. Despite in-plane microwave field excitation, out-of-plane contributions of magnetization precession and dynamic magnetostatic coupling between individual magnetic domains are identified. The amplitude precession is the largest at the dominating precessional frequency mode in agreement with comparative inductive measurements. A phase shift between magnetic field application and induced-domain-wall motion is identified by means of direct imaging. At the magnetic resonance frequency domain-wall precession occurs. Changing the applied bias field, the precessional frequency varies only slightly. Inhomogeneous out-of-phase precessional modes within the individual domains are found close to the bias field of domain annihilation.

The obtained data demonstrate the relevance of detailed magnetic domain knowledge and precise magnetodynamical imaging for the understanding of the dynamic behavior, beyond the elementary adjustment of the high-frequency property of the material.

ACKNOWLEDGMENTS

Funding through the German Research Council (DFG) Grant No. MC9-10/1 is highly appreciated. J.M. thanks the DFG for additional support through Heisenberg Programme. Additional thanks go to A. Gerber and E. Quandt for magnetic film preparation as well as to I. Mönch for pattering of the samples. Special thanks go to R. Knöchel and W. Taute for preparation of the high-bandwidth coplanar waveguides used in the experiments. We thank E. Lage for experimental support.

[1] C. Chappert, A. Fert, and F. N. Van Dau, Nat. Mater. **6**, 813 (2007).
[2] S. Neusser and D. Grundler, Adv. Mater. **21**, 2927 (2009).
[3] V. V. Kruglyak, S. O. Demokritov, and D. Grundler, J. Phys. D: Appl. Phys. **43**, 260301 (2010).
[4] J. Ding, M. Kostylev, and A. O. Adeyeye, Phys. Rev. Lett. **107**, 047205 (2011).
[5] A. Crawford, D. Gardner, and S. Wang, IEEE Trans. Magn. **38**, 3168 (2002).
[6] M. Frommberger, C. Schmutz, M. Tewes, J. McCord, W. Hartung, R. Losehand, and E. Quandt, IEEE Trans. Microwave Theory Techn. **53**, 2096 (2005).
[7] M. Yamaguchi, K. Kim, and S. Ikeda, J. Magn. Magn. Mater. **304**, 208 (2006).
[8] D. S. Gardner, G. Schrom, P. Hazucha, F. Paillet, T. Karnik, and S. Borkar, IEEE Trans. Magn. **43**, 2615 (2007).
[9] H. Wu, D. S. Gardner, W. Xu, and H. B. Yu, IEEE Trans. Magn. **48**, 4123 (2012).

[10] D. A. Thompson and J. S. Best, IBM J. Res. Dev. **44**, 311 (2000).
[11] J. Heidmann, H. Do, M. Xiao, K. Takano, and Y. Ikeda, IEEE Trans. Magn. **42**, 166 (2006).
[12] X. Z. Xing, J. Appl. Phys. **103**, 07F522 (2008).
[13] R. Wood, J. Magn. Magn. Mater. **321**, 555 (2009).
[14] M. A. Escobar, M. V. Lubarda, S. J. Li, R. N. Chang, B. Livshitz, and V. Lomakin, IEEE Trans. Magn. **48**, 1731 (2012).
[15] T. L. Gilbert, IEEE Trans. Magn. **40**, 3443 (2004).
[16] M. Mallary and A. Smith, IEEE Trans. Magn. **24**, 2374 (1988).
[17] K. Ohashi, IEEE Trans. Magn. **21**, 1581 (1985).
[18] B. Webb, M. Re, C. Jahnes, and M. Russak, J. Appl. Phys. **69**, 5611 (1991).
[19] N. Smith, IEEE Trans. Magn. **27**, 729 (1991).
[20] W. Jayasekara, J. Bain, and M. Kryder, IEEE Trans. Magn. **34**, 1438 (1998).
[21] U. Queitsch, J. McCord, A. Neudert, R. Schäfer, L. Schultz, K. Rott, and H. Brückl, J. Appl. Phys. **100**, 093911 (2006).
[22] C. Patschureck, K. Lenz, M. O. Liedke, M. U. Lutz, T. Strache, I. Mönch, R. Schäfer, L. Schultz, and J. McCord, Phys. Rev. B **86**, 054426 (2012).
[23] K. Y. Guslienko, R. W. Chantrell, and A. N. Slavin, Phys. Rev. B **68**, 024422 (2003).
[24] S. Tamaru, J. A. Bain, R. J. M. van de Veerdonk, T. M. Crawford, M. Covington, and M. H. Kryder, Phys. Rev. B **70**, 104416 (2004).
[25] A. Neudert, P. S. Keatley, V. V. Kruglyak, J. McCord, and R. J. Hicken, IEEE Trans. Magn. **44**, 3083 (2008).
[26] M. R. Freeman and B. C. Choi, Science **294**, 1484 (2001).
[27] M. Buess, J. Raabe, C. Quitmann, J. Stahl, and C. H. Back, Surf. Sci. **601**, 5246 (2007).
[28] H. A. Dürr, T. Eimüller, H. J. Elmers, S. Eisebitt, M. Farle, W. Kuch, F. Matthes, M. Martins, H. C. Mertins, P. M. Oppeneer, L. Plucinski, C. M. Schneider, H. Wende, W. Wurth, and H. Zabel, IEEE Trans. Magn. **45**, 15 (2009).
[29] P. Fischer, Mater. Sci. Eng. R-Rep. **72**, 81 (2011).
[30] M. Kryder, P. Koeppe, and F. Liu, IEEE Trans. Magn. **26**, 2995 (1990).
[31] I. Neudecker, K. Perzlmaier, F. Hoffmann, G. Woltersdorf, M. Buess, D. Weiss, and C. H. Back, Phys. Rev. B **73**, 134426 (2006).
[32] D. Chumakov, J. McCord, R. Schäfer, L. Schultz, H. Vinzelberg, R. Kaltofen, and I. Mönch, Phys. Rev. B **71**, 014410 (2005).
[33] A. Neudert, J. McCord, D. Chumakov, R. Schäfer, and L. Schultz, Phys. Rev. B **71**, 134405 (2005).
[34] A. Hubert and R. Schäfer, *Magnetic Domains: The Analysis of Magnetic Microstructures* (Springer, Berlin, 1998).
[35] M. Frommberger, J. McCord, and E. Quandt, IEEE Trans. Magn. **40**, 2703 (2004).
[36] T. Silva, C. Lee, T. Crawford, and C. Rogers, J. Appl. Phys. **85**, 7849 (1999).
[37] T. von Hofe, N. O. Urs, B. Mozooni, T. Jansen, C. Kirchhof, D. E. Bürgler, E. Quandt, and J. McCord, Appl. Phys. Lett. **103**, 142410 (2013).
[38] B. E. Argyle and J. G. McCord, J. Appl. Phys. **87**, 6487 (2000).
[39] C. Kittel, Phys. Rev. **73**, 155 (1948).
[40] S. W. Yuan and H. N. Bertram, J. Appl. Phys. **72**, 1033 (1992).
[41] M. Wolf, R. Schäfer, and J. McCord, J. Magn. Magn. Mater. **321**, 2920 (2009).
[42] C. Patschureck, R. Kaltofen, I. Mönch, R. Schäfer, L. Schultz, and J. McCord, Appl. Phys. Lett. **97**, 052507 (2010).
[43] R. W. Damon and J. R. Eshbach, J. Appl. Phys. **31**, S104 (1960).
[44] K. Y. Guslienko, S. O. Demokritov, B. Hillebrands, and A. N. Slavin, Phys. Rev. B **66**, 132402 (2002).
[45] P. M. Pimentel, B. Leven, B. Hillebrands, and H. Grimm, J. Appl. Phys. **102**, 063913 (2007).
[46] R. Yanes, R. Rozada, F. Garcia-Sanchez, O. Chubykalo-Fesenko, P. M. Pimentel, B. Leven, and B. Hillebrands, Phys. Rev. B **79**, 224427 (2009).
[47] M. Mallary, J. Appl. Phys. **57**, 3952 (1985).